Efficient Waste Management via Tuning Plasma Properties in Radio Frequency Inductively Coupled Plasma

Mustafa A. Aldeeb [1,2]**, Sharif Abu Darda** [1]**, Vahid Damideh** [1]**, Isaac Hassen** [1]
and Hossam A. Gabbar [1,*]**.**

[1] Faculty of Engineering and Applied Science, Ontario Tech University, 2000 Simcoe St. North, ON, L1G0C5, Oshawa, Canada.

[2] National Research Institute of Astronomy and Geophysics (NRIAG), 11421, Helwan, Cairo, Egypt.

* Correspondence: hossam.gaber@ontariotechu.ca

Abstract: In the last ten years, plasma waste treatment has gained increasing prominence as a technology in response to growing challenges in waste disposal and the recognition of opportunities for generating valuable by-products. The efficiency and outcomes of this process are intricately linked to the characteristics of the plasma involved, such as plasma enthalpy and heat flux. We employed an experimental radio frequency inductively coupled plasma (RF-ICP) torch operating at atmospheric pressure to generate plasma. Utilizing optical emission spectroscopy (OES), we measured plasma parameters, specifically the effective electron temperature (T_{eff}) and plasma density (n_e), while varying argon gas flow rates and RF powers. Our investigations revealed that both flow rate and RF power exert significant control over plasma parameters, and we observed an unusual phenomenon within this range of discharge pressures. Consequently, both the plasma's enthalpy and the heat flux it generates are influenced by variations in both flow rate and RF power.

Keywords: RF-ICP torch; optical emission spectroscopy (OES); Boltzmann plot; stark broadening; anomalous skin effect

1. Introduction

Municipal solid waste (MSW) represents the waste generated daily by people, known for its widespread occurrence and intricate composition. The significant increase in waste production can be attributed to the processes of urbanization and industrialization. The practice of mass burn incineration has traditionally been a prominent thermal method for managing MSW [1,2]. There are more than 1400 operational incineration facilities globally, and many more are in the process of being commissioned for waste-to-energy applications [3]. However, the overall energy efficiency of contemporary incineration plants remains relatively low, typically falling within the range of 22% to 25%. This is primarily due to the necessity of maintaining lower steam temperatures, usually around 450°C, to safeguard equipment from corrosion induced by acidic gases like HCl [4]. Consequently, the demand for excessive airflow constrains the achievable temperature within the incineration process chamber, leading to the production of hazardous pollutants, including chlorinated dioxins and furans. These contaminants contribute to air pollution and are linked to severe health concerns such as cancer and developmental abnormalities [5]. Despite the incorporation of state-of-the-art technologies for environmentally friendly waste disposal in modern incineration plants, the potential for generating toxic gases remains a subject of debate [6]. The highest likelihood of dioxin formation occurs within the temperature range of 350 to 400°C [7]. To address the negative environmental impacts associated with incineration, alternative technologies like pyrolysis and gasification have emerged as practical options. These methods have demonstrated their ability to reduce the generation of dioxins and furans to acceptable levels [8]. Among these alternatives, gasification is considered more efficient for large-scale waste disposal. However, it does produce unwanted byproducts, such

as tar, in addition to desired outcomes like syngas, producer gas, and char [9]. The presence of tar in the product gas can lead to various adverse effects, including diminished product quality, fouling of pipelines, corrosion, and deactivation of catalysts [10]. In this context, thermal plasma technology stands out as the singular thermal waste treatment process capable of effectively managing diverse waste types, including hazardous materials, while converting waste into valuable products without harming the environment [11]. It offers a range of advantages over conventional methods, which encompass exceptional destruction efficiency (with volume reduction surpassing 99%), the removal of harmful molecules, decreased CO_2 emissions, and the production of high-calorific value gas [12,13]. By virtue of its high-temperature heat source and the presence of charged particles, plasma fosters increased reactivity within the environment. This, in turn, promotes the decomposition of tar and augments the rate at which tar is eliminated [14,15]. The adoption of thermal plasma technology has been on the rise and is being implemented in countries such as the UK, USA, Canada, Belgium, and India, where it serves as a waste-to-energy solution for electricity generation, with capacities reaching up to 100 MW [16]. The realm of plasma-assisted waste processing technology is broadly categorized into two methods: plasma pyrolysis and plasma gasification. In plasma gasification, waste is subjected to a controlled quantity of oxygen, while plasma pyrolysis involves decomposing waste in an oxygen-deprived environment [5,12,17]. In the context of thermal treatment, an air supply of less than or equal to 5% relative to stoichiometric air can be considered to lead to pyrolysis conditions for waste treatment [18]. Numerous studies, ranging from laboratory to pilot-scale, have been conducted to explore the environmental and output implications of employing plasma pyrolysis technology for waste management. A wide array of waste materials, including polyethylene, polypropylene, rubber, tires, biomass, paper, refuse-derived fuel, and medical waste, have been treated using different power sources, such as DC, AC, RF, and Microwave, with power supply capacities ranging from 0.8 to 50 kW. In all instances, the primary composition of explosive products comprises H_2 and CO. The concentration of pollutants like CO_2 varies from 2% to 15%, while solid residues, taking the form of carbon black, slag, or ash, fall within the range of 6% to 40% [19,20]. Initially, it has reported that the eco-friendly treatment of medical waste using plasma pyrolysis technology necessitates an energy consumption of approximately one kWh per kg [13]. Furthermore, Plasma Gasification Melting technology has been employed to convert MSW at a rate of 300 kg/h into syngas with energy content ranging from 6 to 7 MJ/Nm^3. In this process, steam feed rates vary from 70 to 100 kg/h, and plasma power consumption ranges from 0.8 to 0.87 kWh/kg [21]. Stringent environmental regulations have created opportunities for plasma pyrolysis technology to emerge as a highly viable option for managing MSW and other solid wastes, ensuring minimal environmental impacts.

Thermal plasma refers to a high-temperature plasma operating at elevated pressures, typically close to atmospheric levels. It is characterized by high power and current densities within the plasma, resulting in significant enthalpy. This property allows thermal plasma to efficiently heat injected materials and electrodes. As a result of its exceptional heat capacity, thermal plasma finds widespread use in applications like arc welding, plasma arc cutting, waste disposal, and more. In some cases, thermal plasma can be generated not only between electrodes but also through inductive coupling, giving rise to what is known as inductively coupled thermal plasma (ICTP) [22]. Reed originally developed the fundamental configuration of ICTP in the 1960s [23]. It involves the establishment of plasma within a cylindrical dielectric tube encircled by an induction coil. Radiofrequency (RF) current flowing through the coil generates electromagnetic fields, which, in turn, accelerate electrons within the torch, thus creating plasma. When operating at high pressures, typically near atmospheric levels, the plasma assumes a thermal state, with gas temperatures reaching several thousand Kelvins, closely aligned with electron temperatures. One of the most significant advantages of ICTP is its ability to generate a clean, high-temperature environment free from contamination by electrode materials. Capitalizing on these benefits, ICTPs have found diverse applications, including waste disposal [24], thermal barrier coating production [25–27], diamond film deposition [28], fullerene synthesis [29,30], fine powder spheroidization [31–33], nanopowder synthesis [34–37], nanotube production [38,39], catalyst synthesis [40], and astrophysical research

[41]. Despite the successful utilization of ICTP torches in numerous material processes, certain limitations have also emerged. These include challenges related to stable operation in the presence of disturbances, counterflows within the circulating gas, reduced power efficiency, and difficulties in controlling gas temperatures [42].

Therefore, examining plasma properties, such as plasma density and electron temperature, is essential for developing and improving the RF-ICP torches. OES is a non-intrusive and powerful tool to investigate plasma properties and gives rich information about energy states. The OES measurements can calculate and determine plasma temperature (T_e), species density, plasma composition, and ionization state. Numerous studies using the OES method to examine the plasma jet's characteristics have recently been conducted [43–47]. Despite significant research and advancements in this field, a more profound comprehension of a plasma jet's characteristics is still required. This is important for investigations into a newly developed plasma torch with a unique configuration that aims to enhance and optimize performance. The consequences of plasma processing will be significantly influenced by these characteristics, which are connected to the underlying physical processes of the plasma sources.

This research endeavors to conduct a comprehensive examination of the essential features and optimal operational parameters of a newly developed RF-ICP torch, specifically designed for small-scale municipal solid waste (MSW) pyrolysis, with the aim of enhancing and refining RF torch devices. A previous study extensively investigated the composition and properties of the waste material [48]. To gain insights into the fundamental characteristics of the plasma source, we employed OES to capture and analyze argon plasma spectra outside the plasma chamber. We determined electron number densities through the Stark broadening of ArI lines and calculated the excitation temperatures of the plasma jet using the Boltzmann plot technique. Section II provides a comprehensive explanation of the experimental setup for the RF-ICP plasma torch. The results of the OES measurements performed on the RF-ICP plasma torch are documented in Section III, along with an elaboration of the methodology for computing electron temperature, species densities, and plasma temperature. These properties, along with the underlying physical phenomena of the plasma sources, will significantly influence the outcomes of plasma processing.

2. Material and Methods

The inductively coupled plasma (ICP) torch is composed of various elements. It incorporates a copper plasma gas flow diffuser head fitted with two central copper tubes, each having a 6mm inner diameter and an 8mm outer diameter for introducing the plasma-forming gas. Additionally, there are two plasma igniter pins (high voltage feed) mounted on top of the diffuser head to ignite the plasma. To maintain a separation between the plasma and the chamber wall, a high-flow sheath gas inlet tube, made of copper, is connected to one side of the copper torch heads. The plasma chamber itself is constructed with a central quartz tube measuring 18mm in outer diameter, 1.5mm in thickness, and extending for a length of 90mm. It is encased by a sheath quartz tube with an outer diameter of 25mm, a thickness of 2.5mm, and a length of 180mm. This outer quartz tube is surrounded by an isolated water-cooled copper coil consisting of seven turns. The plasma chamber and RF coil are housed within a Teflon shielding cylinder. The RF power is supplied to the coil through an Advanced Energy generator (Model RFX3000), capable of delivering a maximum power output of 1.1 kW and operating at a nominal frequency of 13.56 MHz.

OES data was gathered at different gas flow rates and RF powers using the Ocean Insight Flame-S-XR1-ES spectrometer, which offers a resolution of 1.7 nm through an optical fiber with a length of 1.5 m and an integration time of 1 ms. To assess the instrument's spectral broadening, a diode-pumped solid-state laser line (660 nm) was utilized, yielding a value of ($\Delta\lambda_I$) = 0.66 nm. It's important to note that, throughout the optical measurements, only argon gas was introduced through one of the central tubes. A visual representation of the experimental configuration featuring the RF-ICP plasma torch is depicted in Figure 1.
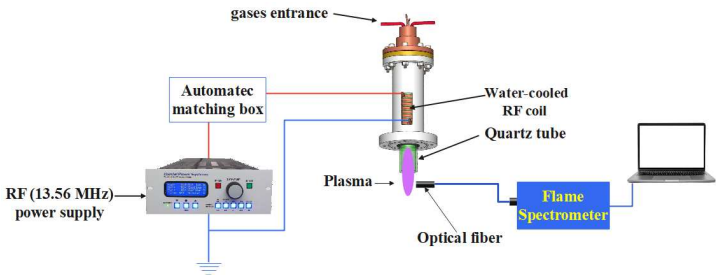
Figure 1. Experimental setup of the Ar spectrum measurements.

3. Results

One of the key benefits of employing RF-ICP discharge in various applications is its capacity to produce high-density plasma [49]. Within the RF-ICP discharge, it's primarily the electrons that play a pivotal role in driving the excitation and ionization processes occurring in the discharge. This is because only electrons can swiftly navigate the rapidly changing electric field. In contrast, ions within the RF discharge are less influential and do not significantly contribute to the RF plasma discharge due to their limited mobility [50]. The high-frequency magnetic field in RF-ICP serves as the driving force for accelerating electrons, elevating their energy levels significantly. Among these energized electrons, those possessing energy exceeding 13 eV undergo collisions with ground state argon atoms, thereby inducing a transition from their base state to an excited state. When these argon atoms exist in either the excited state Ar* or higher excited state Ar**, their return to a metastable state or resonance energy level results in the emission of light. This sequence of events is mathematically represented by the following equations [43]:

$$e + Ar \rightarrow Ar^* + e \qquad (1)$$
$$Ar^* \rightarrow Ar + h\nu \qquad (2)$$
$$e + Ar \rightarrow Ar^{**} + e \qquad (3)$$
$$Ar^{**} \rightarrow Ar + h\nu \qquad (4)$$

OES analysis of the Ar RF-ICP discharge encompassed wavelengths ranging from 400-950 nm and different ranges of power 440, 550, 660, 770, 880, 990, and 1100 W and argon gas flow rates 2 and 4 standard liters per minute (SLPM). In figure 2 (a, b), the emission spectrum of the atmospheric pressure Ar RF-ICP is depicted, observed under specific conditions involving an applied power of 440 watts and Ar gas flow rates of 2 and 4 SLPM, respectively. The spectral lines detected within the wavelength range of 696.53 to 852.14 nm primarily originated from excited atomic species denoted as Ar* (first excited state of Ar).

Within the Ar RF-ICP discharge, a total of eighteen atomic lines spanning from 696.53 to 852.14 nm were identified. Table 1 provides a compilation of the parameters associated with these atomic lines, sourced from NIST. The intensity of the line could show a direct correlation with the quantity of atoms in the excited state. Subsequent discussions delve into the patterns of intensity variation for these lines under various plasma conditions.

Table 1. The wavelength, excitation energy (Ek), transition probability (Aik), and statistical weight (gk) for the appeared lines in the region of 696-851 nm.

λ (nm)	E_k (eV)	A_{ik} (10^6 S^{-1})	g_k
696	13.328	6.40	3
706	13.302	3.80	5
727	13.328	1.83	3
738	13.302	8.50	5
750	13.479	45	1
751	13.273	40	1
763	13.172	24	5
771	13.153	5.20	3

772	13.328	11.7	3
794	13.283	18.6	3
800	13.172	49	5
801	13.095	9.30	5
810	13.153	25	3
811	13.076	33	7
826	13.328	15.3	3
840	13.302	22.3	5
842	13.095	21.5	5
851	13.283	13.9	3
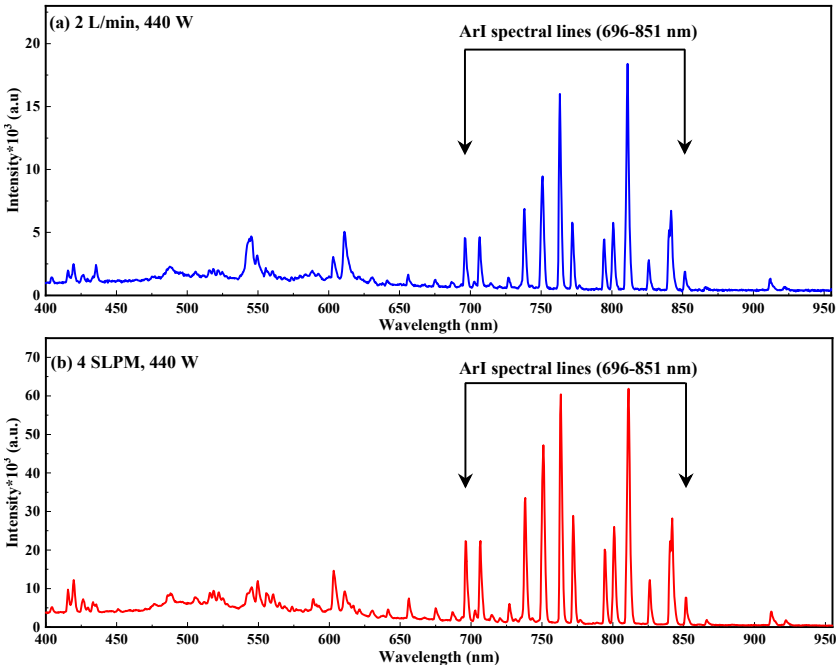
Figure 2. (a) Argon emission spectra at flow rate 2 SLPM and 440 RF power. (b) Argon emission spectra at flow rate 4 SLPM and 440 RF power.

Ar* lines were examined under varying applied RF power levels of 440, 550, 660, 770, 880, 990, and 1100 W, with corresponding gas flow rates of 2 and 4 SLPM in figure 3 (a, b). At 2 SLPM gas flow rate (refer to figure 3a), it is evident that the intensities of all Ar* lines exhibit a consistent increase with escalating RF power. This behavior can be attributed to the heightened efficiency of the plasma in generating Ar* atoms as the RF power is increased, resulting in intensified line emissions. Conversely, when considering a gas flow rate of 4 SLPM (as shown in figure 3b), the intensities initially decrease with increasing RF power up to 770 W and subsequently stabilize. In this scenario, the creation of excited atoms diminishes initially and reaches a point of equilibrium as RF power increases. To gain deeper insights into these phenomena, plasma electron temperature and plasma density calculations were conducted and will be elaborated upon in the subsequent discussion.
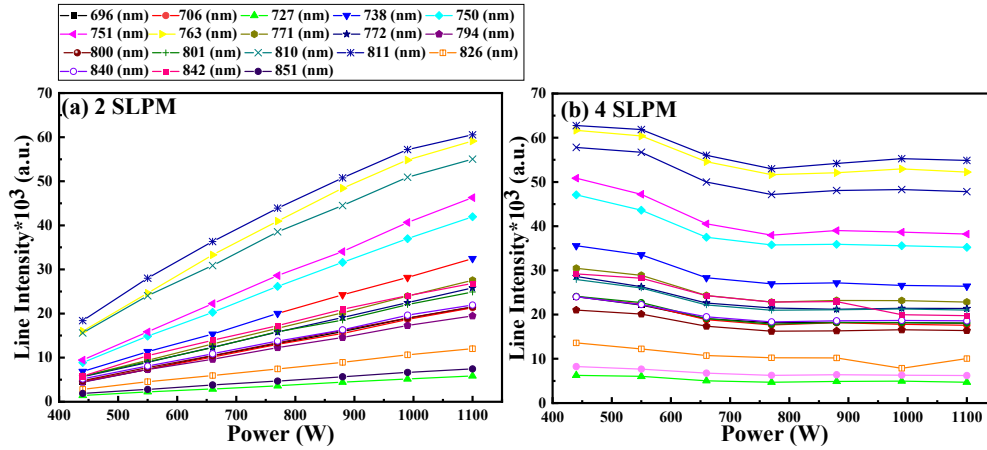
Figure 3. (a) shows the Ar* lines intensity variation with the RF power at 2 SLPM. (b) shows the Ar* lines intensity variation with the RF power at 4 SLPM.

3.1. Excitation temperature

Boltzmann plot was used to determine the effective electron temperature (Teff) (eV) for the plasma produced from RF-ICP torch using the following equation:

$$ln(\frac{I_{ki}\lambda_{ki}}{A_{ki}g_k}) = -\frac{E_k}{k_B T_{eff}} + C \tag{5}$$

where λ_{ki}, A_{ki}, E_k, and g_k are wavelength (nm), transition probability (S-1), excitation energy (eV), and statistical weight of the upper state, respectively, kB is the Boltzmann constant, and C is a constant. By plotting the left-hand side of Eq. 5 [$ln(\frac{I_{ki}\lambda_{ki}}{A_{ki}g_k})$] on the vertical axis and Ek on the horizontal axis, the Teff can be derived from the inverse of the slope of the linear fitted line. The Boltzmann plot is an efficient method for determining Teff in atmospheric plasma torches; since it does not require a standard source for calibration, and the accuracy increases with the energy range of the emitted lines used in the calculations [51–53]. All lines in Table 1 are well isolated and unabsorbed and were chosen to implement the Boltzmann plot. Boltzmann plot for flow rates of 2 and 4 SLPM and RF power 440 W displayed in figure 4 (a, b), respectively. The error in determination of electron temperature is around 20 % and it is generated from the uncertainty in the determination of transition probability (Aki) of the Ar* lines and experimental uncertainty [51].
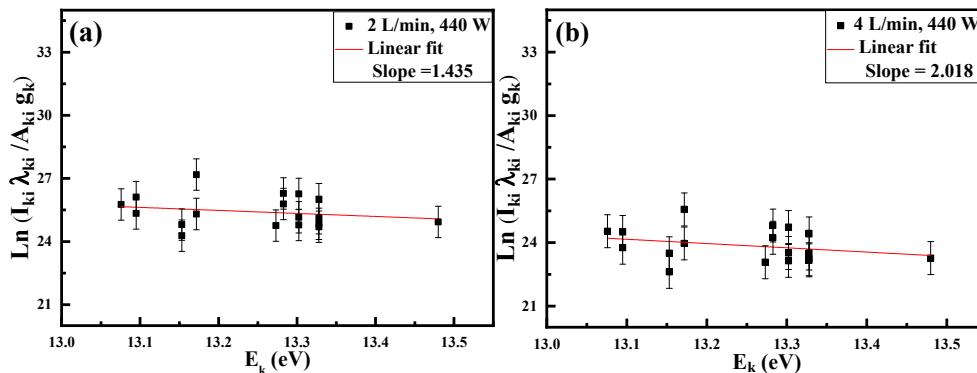
Figure 4. (a) shows Boltzmann plot for emission lines at flow rate 2 SLPM and 440 W RF power. (b) shows Boltzmann plot for emission lines at flow rate 4 SLPM and 440 W RF power.

The relationship between electron temperature, RF power, and gas flow rate is a widely recognized phenomenon. Typically, electron temperature decreases as RF power increases due to the amplified influence of the two-stage ionization process and electron-electron interactions, which are more pronounced at higher plasma densities [54–57]. Simultaneously, electron temperature decreases

as gas flow rate increases; the heightened gas flow rate results in a greater number of gas atoms, leading to increased electron-atom collision probability, thereby increasing plasma density, and reducing electron temperature [58]. Figure 5 illustrates this behavior. At a gas flow rate of 2 SLPM, the electron temperature exhibits the expected trend, decreasing with increasing RF power. However, at 4 SLPM, the behavior of electron temperature is contrary to the norm. Initially, it is lower than the value observed at 2 SLPM, but as RF power increases.
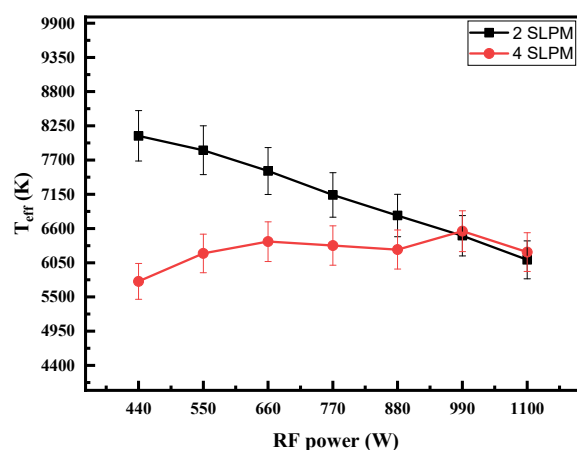
Figure 5. Electron temperature variation with RF power at 2 and 4 SLPM Ar gas flow rates.

The inverse behavior of the electron temperature at 4 SLPM is due to the anomalous skin effect [56]. Only a few electrons significantly contribute to the current density in the anomalous skin effect. These are "glancing" electrons, which spend a significant portion of the field period inside the skin layer after being reflected at modest angles from the plasma barrier. The remaining electrons leave the epidermal layer too quickly to contribute much to the current [59].

The RF-ICP torch is operated in a non-propagating regime. The driving RF field only displays a skin effect by penetrating the plasma within a skin layer (δ) near the antenna [49]. The surface of the plasma is where the induced electric current and radio frequency field are concentrated. Due to electrons' higher mobility than ions, only electrons are responsible for energy transfer and ionization. The electrons gain energy from the electric field in the skin layer and transfer this energy to the gas atoms to generate more charges and increase the energy conversion rate of the material. Reducing the charge density reduces the efficiency of the torch during the treating process. The charges can be lost by diffusing the energetic electrons to the reactor walls or creating only excited atoms. One solution developed to reduce electron loss through the chamber wall is to provide an axially high flow of Ar gas to form a cooled barrier gas that separates the plasma from the walls. Vortex flow has the same effect as axially high flow [22]. At 4 SLPM, another energy loss mechanism was detected due to the anomalous skin effect. Most of the electrons with sufficient energy did not contribute to the ionization of the atoms to increase the current density. Therefore, the charge density decreases, as does the energy efficiency of the torch. Anomalous skin is an uncontrollable phenomenon that we can only detect and try to avoid.

3.2. Electron density

The measurement of plasma density (ne) is a crucial parameter for assessing energy transfer efficiency in the torch and for determining the state of ionization equilibrium. There are two main approaches to calculate electron density: electrical diagnostics and optical diagnostics. The use of Langmuir probes (single, double, and triple probes) for electron density calculation, which falls under electrical diagnostics, is less accurate at atmospheric pressure where the plasma experiences high collision conditions [60]. On the other hand, the Stark broadening method, a widely employed optical diagnostics technique for electron density calculation [44,60–62], offers a more cost-effective and accessible alternative compared to methods like Thomson scattering or laser heterodyne

interferometry. Its accuracy is notably high within the range of plasma density around 1016 cm-3 [60].

The broadening of the spectra line (FWHM) ($\Delta\lambda_{exp}$) (nm) is a convolution of the Lorentzian profile (Stark, Van der Waals, and Resonance broadening) and Gaussian profile (Doppler and instrumental boarding):

$$\Delta\lambda_{exp} = 0.5\Delta\lambda_L + \sqrt{(0.5\Delta\lambda_L)^2 + (\Delta\lambda_G)^2} \tag{6}$$

In our experiment conditions (pressure and Te $\cong$10000 K), both Resonance broadening and Van Der Waals broadening are negligible [45,55]. The following equation represents the Gaussian profile:

$$\Delta\lambda_G = \sqrt{\Delta\lambda_I^2 + \Delta\lambda_D^2} \tag{7}$$

where $\Delta\lambda_I$ (nm) is the instrumental broadening and $\Delta\lambda_D$ (nm) is Doppler broadening. Doppler broadening is given by:

$$\Delta\lambda_D = 7.156 \times 10^{-7}\lambda_o\left(\frac{T_g}{M_A}\right)^{\frac{1}{2}} \tag{8}$$

where λo, T_g, and M_A are the wavelength (nm), the gas temperature (K), and the mass of the emitter (Kg), respectively. By using a Voigt function for deconvolution, we can calculate the Stark broadening ($\Delta\lambda_s$) (nm) from Eq. 6, and the electron density can be calculated using the empirical formula [60]:

$$ln\,N_e = 46.516 + 0.992\,ln\,\Delta\lambda_s - 0.612\,ln\,T_{eff} \tag{9}$$

where N_e, $\Delta\lambda_s$, and T_{eff} are the plasma density (cm -3), Stark broadening (nm), and electron temperature (eV).

This research utilized a distinct, non-absorptive Ar* line at 738.3 nm to estimate the plasma density. By fitting the experimental data with the Voigt function using Origin software, as can be seen in Figure 6 (a-f), the FWHM ($\Delta\lambda_{exp}$) (nm) of this line is obtained.
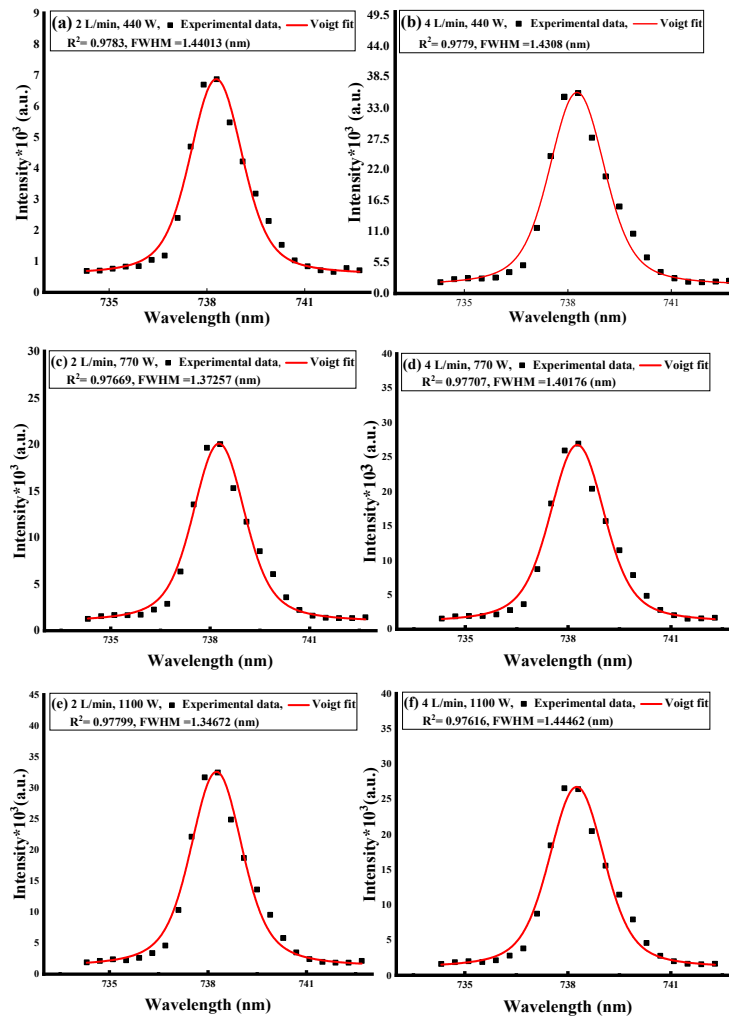
Figure 6. (a, c, e) Ar* (738.3 nm) line fitted with Voigt function at flow rate 2 SLPM and 440, 770, 1100 RF powers, respectively. (b, d, f) Ar* (738.3 nm) line fitted with Voigt function at flow rate 4 SLPM and 440, 770, 1100 RF powers, respectively.

Doppler broadening $\Delta\lambda_D$ = 0.008 nm was calculated from Eq. 8 at $T_g \cong 10,000$ K, and the instrumental broadening $\Delta\lambda_I$ = 0.66 nm was measured by using a diode-pumped solid-state laser line (660 nm). Table 2 shows $\Delta\lambda_{exp}$, and $\Delta\lambda_S$, at different RF power and flow rates extracted from the fitting and calculated from Eq. 6.

Table 2. contains measured $\Delta\lambda_{exp}$ of the Ar* line 738.3 nm and the calculated $\Delta\lambda_S$.

2 SLPM			4 SLPM		
Power (W)	$\Delta\lambda_{exp}$ (nm)	$\Delta\lambda_s$ (nm)	Power (W)	$\Delta\lambda_{exp}$ (nm)	$\Delta\lambda_s$ (nm)
440	1.431	1.126	440	1.440	1.138
550	1.406	1.096	550	1.358	1.037
660	1.415	1.108	660	1.461	1.162
770	1.402	1.091	770	1.372	1.055
880	1.377	1.061	880	1.363	1.044
990	1.436	1.133	990	1.419	1.113
1100	1.445	1.143	1100	1.346	1.023

Using Eq. 9, we determined the plasma density and graphically represented the relationship between electron density, power, and gas flow rate. The limit of error in plasma density computations was 15% stand for measurements uncertainty [1,52]. Figure 7 illustrates the correlation between plasma density and RF power for gas flow rates of 2 and 4 SLPM. Typically, an increase in RF power and gas flow rate results in higher plasma density [54–57]. However, Figure 7 demonstrates an unexpected pattern. At 4 SLPM, plasma density decreases as RF power increases. This aligns well with the electron temperature findings.
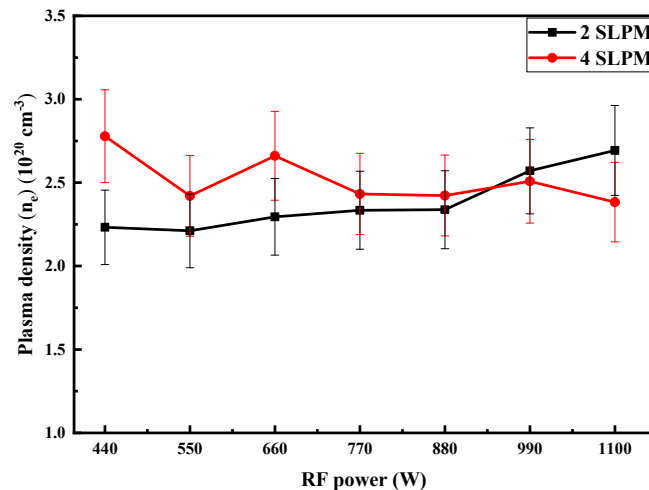
Figure 7. Shows the variation of the plasma density (ne) with RF power at two different Ar flow rates 2 and 4 SLPM.

The relationship between current density (J) and electron density (n_e) in a plasma can be described by the conductivity (σ) of the plasma. Specifically, Ohm's law for a plasma relates current density to electron density and electrical conductivity as follows [63]:

$$J = \sigma \cdot E \qquad (10)$$

where J is the current density (A/m^2), σ is the electrical conductivity of the plasma (S/m), and E is the electric field strength (V/m).

The electrical conductivity (σ) of a plasma depends on several factors, including electron density n_e, electron mobility (μ_e), and charge of an electron (e). The relationship can be expressed as:

$$\sigma = n_e \cdot \mu_e \cdot e \tag{11}$$

where ne is the electron density (m^{-3}), μ_e is the electron mobility ($m^2/V \cdot s$), and e is the elementary charge of an electron ($\approx 1.60217663 \times 10{-}19$ C).

From Eq. 10, 11, that current density is directly proportional to electron density. Therefore, as the electron density in a plasma increases, assuming other factors remain constant, the current density also increases.

In atmospheric plasma, a condition known as Local Thermodynamic Equilibrium (LTE) prevails, where the electron temperature, gas temperature, and ion temperature closely align with one another. The enthalpy of the plasma jet is dependent on the electron temperature, and it rises as the electron temperature increases [64]. Conversely, the energy transferred from the electrical source to the waste is contingent upon the plasma density [65]. Utilizing plasma technology for treatment of MSW serves a dual purpose: it aims to reduce the waste's volume for environmental reasons and yields valuable products like syngas for energy production and useful by-products such as carbon black and carbon nanospheres [66]. The efficiency of this process is closely linked to the properties of the plasma itself. Factors like the conversion rate, the heating value of the generated gas, and the characteristics and types of by-products produced are all dependent on the properties of the plasma. It was observed that the conversion rate increases as the plasma current rises, as higher-density plasma enhances heat transfer and energy exchange with the waste material, ultimately reducing its volume [66]. Additionally, a high plasma current results in the production of carbon black and a significant quantity of nano-sized spherical particles, which are comparable to commercial-grade materials [66]. However, it should be noted that an increase in plasma current leads to a decrease in the calorific value of the generated gas [65]. Greater plasma enthalpy yields higher proportions of H_2 and CO, while decreasing the presence of heavy hydrocarbons and enhancing slag formation [66,67].

4. Conclusion

We have developed an atmospheric RF-ICP torch for the small-scale pyrolysis of mixed waste materials, primarily consisting of paper and polypropylene. Our earlier research extensively characterized the waste material, pinpointing its maximum degradation temperature (ranging from 369.55 to 447.88 °C) and thermal stability (between 381.60 and 393.82 °C). The main objective of this study was to identify the optimal operational conditions that yield a stable plasma with properties conducive to maximizing profits and efficiency in the pyrolysis process. Given the challenges associated with studying high-temperature plasma, OES was employed to investigate plasma parameters under varying RF power and gas flow rates of 2 and 4 SLPM. Our findings revealed that electron temperature decreased with RF power at a 2 SLPM gas flow rate but increased with RF power at the 4 SLPM rate. Stark broadening calculations substantiated an increase in plasma density with higher RF power, ranging from 2.231×10^{20} - 2.693×10^{20} cm^{-3}.

The enthalpy of the plasma jet depends on the plasma temperature, whereas the heat flux generated by the plasma is linked to the plasma density. Consequently, adjustments in the RF power and flow rate of the plasma have a profound impact on these properties, and these alterations will be mirrored in the material processing. Variations in flow rate and RF power will lead to changes in the conversion rate, calorific value of the produced gas, process duration, by-product characteristics, and formation.

For small- or large-scale pyrolysis of mixed waste materials, the use of the proposed atmospheric RF-ICP torch showed significant impacts on sustainable development in community applications. This groundbreaking study provides a sustainable alternative by turning paper and polypropylene waste into useful resources using optimized plasma torches. In addition, plasma-based pyrolysis addresses the challenges of mixed waste with effective thermal management and energy efficiency. This work emphasizes a critical component of sustainable waste management by determining ideal operating conditions through an extensive examination of plasma characteristics utilizing OES.

This study has far-reaching consequences beyond its immediate technological breakthroughs. By providing a solution for reducing environmental stressors related to trash disposal, it adds to the broader framework of sustainable development. The pyrolysis process may be made more efficient and effective by varying the gas flow rates and RF power to accurately regulate the plasma characteristics. By turning trash into valuable goods such as syngas or useful chemicals, the proposed optimal technique will limit environmental pollution, will reduce waste volume, and will promote the circular economy.

Moreover, the knowledge derived from the correlation between plasma parameters and material processing results offers a guide for developing waste treatment methods that are more ecologically friendly and efficient. Because changes in flow rate and RF power have a direct effect on the formation, by-product characteristics, process duration, calorific value of produced gas, and conversion rate, this research opens the door to customized waste treatment procedures that optimize resource recovery while reducing environmental impact.

The study's conclusions provide a framework for the creation of sustainable waste management plans that complement international initiatives aimed at creating a more resource- and circular-efficient economy. The knowledge gained from this study not only advances the field of plasma-based waste treatment but also makes a substantial contribution to the larger objectives of sustainable development, highlighting the significance of cutting-edge technology in tackling urgent environmental issues.

In our forthcoming research, we will integrate the torch into a small-scale pyrolysis system and empirically investigate the influence of RF power, flow rate, plasma temperature, and plasma density on the outcomes of the process. Additionally, we aim to develop a waste treatment strategy based on plasma that is specifically tailored for this type of waste.

References

1. Lombardi, L.; Carnevale, E.; Corti, A. A Review of Technologies and Performances of Thermal Treatment Systems for Energy Recovery from Waste. *Waste Management* **2015**, *37*, 26–44, doi:10.1016/J.WASMAN.2014.11.010.
2. Brunner, P.H. WTE: Thermal Waste Treatment for Sustainable Waste Management. In *Recovery of Materials and Energy from Urban Wastes*; Springer New York: New York, NY, 2019; pp. 523–536.
3. Leckner, B. Process Aspects in Combustion and Gasification Waste-to-Energy (WtE) Units. *Waste Management* **2015**, *37*, 13–25, doi:10.1016/J.WASMAN.2014.04.019.
4. Panepinto, D.; Tedesco, V.; Brizio, E.; Genon, G. Environmental Performances and Energy Efficiency for MSW Gasification Treatment. *Waste Biomass Valorization* **2015**, *6*, 123–135, doi:10.1007/S12649-014-9322-7/METRICS.
5. Manisalidis, I.; Stavropoulou, E.; Stavropoulos, A.; Bezirtzoglou, E. Environmental and Health Impacts of Air Pollution: A Review. *Front Public Health* **2020**, *8*, 505570, doi:10.3389/FPUBH.2020.00014/BIBTEX.
6. Dong, J.; Tang, Y.; Nzihou, A.; Chi, Y.; Weiss-Hortala, E.; Ni, M. Life Cycle Assessment of Pyrolysis, Gasification and Incineration Waste-to-Energy Technologies: Theoretical Analysis and Case Study of Commercial Plants. *Science of The Total Environment* **2018**, *626*, 744–753, doi:10.1016/J.SCITOTENV.2018.01.151.
7. Safavi, S.M.; Richter, C.; Unnthorsson, R. Dioxin and Furan Emissions from Gasification. In *Gasification*; Silva, V., Tuna, C.E., Eds.; IntechOpen: Rijeka, 2021; p. Ch. 5 ISBN 978-1-83968-796-9.
8. Lopes, E.J.; Okamura, L.A.; Yamamoto, C.I. FORMATION OF DIOXINS AND FURANS DURING MUNICIPAL SOLID WASTE GASIFICATION. *Brazilian Journal of Chemical Engineering* **2015**, *32*, 87–97, doi:10.1590/0104-6632.20150321S00003163.
9. Magoua Mbeugang, C.F.; Li, B.; Lin, D.; Xie, X.; Wang, S.; Wang, S.; Zhang, S.; Huang, Y.; Liu, D.; Wang, Q. Hydrogen Rich Syngas Production from Sorption Enhanced Gasification of Cellulose in the Presence of Calcium Oxide. *Energy* **2021**, *228*, 120659, doi:10.1016/J.ENERGY.2021.120659.
10. Cortazar, M.; Santamaria, L.; Lopez, G.; Alvarez, J.; Zhang, L.; Wang, R.; Bi, X.; Olazar, M. A Comprehensive Review of Primary Strategies for Tar Removal in Biomass Gasification. *Energy Convers Manag* **2023**, *276*, 116496, doi:10.1016/J.ENCONMAN.2022.116496.
11. Yadav, A.; Karmakar, S.; Kar, S.; Kumar, M. Numerical Modelling of a Direct Current Non-Transferred Thermal Plasma Torch for Optimal Performance. *Contributions to Plasma Physics* **2023**, *63*, e202200088, doi:10.1002/CTPP.202200088.
12. Li, J.; Liu, K.; Yan, S.; Li, Y.; Han, D. Application of Thermal Plasma Technology for the Treatment of Solid Wastes in China: An Overview. *Waste Management* **2016**, *58*, 260–269, doi:10.1016/j.wasman.2016.06.011.

13. Nema, S.K.; Ganeshprasad, K.S. Plasma Pyrolysis of Medical Waste. *Curr Sci* **2002**, *83*, 271–278.

14. Bosmans, A.; Vanderreydt, I.; Geysen, D.; Helsen, L. The Crucial Role of Waste-to-Energy Technologies in Enhanced Landfill Mining: A Technology Review. *J Clean Prod* **2013**, *55*, 10–23, doi:10.1016/j.jclepro.2012.05.032.

15. Rueda, Y.G.; Helsen, L. The Role of Plasma in Syngas Tar Cracking. *Biomass Convers Biorefin* **2020**, *10*, 857–871, doi:10.1007/S13399-019-00461-X/METRICS.

16. Mostaghimi, J.; Boulos, M.I. Thermal Plasma Sources: How Well Are They Adopted to Process Needs? *Plasma Chemistry and Plasma Processing* **2015**, *35*, 421–436, doi:10.1007/S11090-015-9616-Y/METRICS.

17. Munir, M.T.; Mardon, I.; Al-Zuhair, S.; Shawabkeh, A.; Saqib, N.U. Plasma Gasification of Municipal Solid Waste for Waste-to-Value Processing. *Renewable and Sustainable Energy Reviews* **2019**, *116*, 109461, doi:10.1016/j.rser.2019.109461.

18. Pancholi, K.C.; Sen, N.; Singh, K.K.; Vincent, T.; Kaushik, C.P. Transient Heat Transfer during Startup of a Thermal Plasma Chamber: Numerical Insights. *Progress in Nuclear Energy* **2022**, *152*, 104371, doi:10.1016/J.PNUCENE.2022.104371.

19. Tang, L.; Huang, H. SOME OBSERVATIONS FROM STUDIES OF RF PLASMA PYROLYSIS OF WASTE TIRES. *Chem Eng Commun* **2010**, *197*, 1541–1552, doi:10.1080/00986445.2010.485013.

20. Khongkrapan, P.; Thanompongchart, P.; Tippayawong, N.; Kiatsiriroat, T. Microwave Plasma Assisted Pyrolysis of Refuse Derived Fuels. *Central European Journal of Engineering* **2014**, *4*, 72–79, doi:10.2478/S13531-013-0142-5/MACHINEREADABLECITATION/RIS.

21. Zhang, Q.; Dor, L.; Fenigshtein, D.; Yang, W.; Blasiak, W. Gasification of Municipal Solid Waste in the Plasma Gasification Melting Process. *Appl Energy* **2012**, *90*, 106–112, doi:10.1016/J.APENERGY.2011.01.041.

22. Boulos, M.I.; Fauchais, P.L.; Pfender, E. The Plasma State. *Handbook of Thermal Plasmas* **2016**, 1–53, doi:10.1007/978-3-319-12183-3_1-2.

23. Reed, T.B. Induction-Coupled Plasma Torch. *J Appl Phys* **1961**, *32*, 821–824, doi:10.1063/1.1736112.

24. Fazekas, P.; Czégény, Z.; Mink, J.; Bódis, E.; Klébert, S.; Németh, C.; Keszler, A.M.; Károly, Z.; Szépvölgyi, J. Decomposition of Poly(Vinyl Chloride) in Inductively Coupled Radiofrequency Thermal Plasma. *Chemical Engineering Journal* **2016**, *302*, 163–171, doi:10.1016/J.CEJ.2016.05.044.

25. Major, K.; Veilleux, J.; Brisard, G. Lithium Iron Phosphate Powders and Coatings Obtained by Means of Inductively Coupled Thermal Plasma. *Journal of Thermal Spray Technology* **2016**, *25*, 357–364, doi:10.1007/S11666-015-0289-0/METRICS.

26. Darthout, É.; Gitzhofer, F. Thermal Cycling and High-Temperature Corrosion Tests of Rare Earth Silicate Environmental Barrier Coatings. *Journal of Thermal Spray Technology* **2017**, *26*, 1823–1837, doi:10.1007/S11666-017-0635-5/METRICS.

27. Darthout, É.; Gitzhofer, F. Structure Stabilization by Zirconia Pinning Effect of Y2Si2O7 Environmental Barrier Coatings Synthesized by Solution Precursor Plasma Spraying Process. *Surf Coat Technol* **2017**, *309*, 1081–1088, doi:10.1016/J.SURFCOAT.2016.10.015.

28. Berghaus, J.O.; Meunier, J.L.; Gitzhofer, F. Monitoring and Control of RF Thermal Plasma Diamond Deposition via Substrate. *Meas Sci Technol* **2003**, *15*, 161, doi:10.1088/0957-0233/15/1/023.

29. Todorovic-Marković, B.; Marković, Z.; Mohai, I.; Károly, Z.; Gál, L.; Föglein, K.; Szabó, P.T.; Szépvölgyi, J. Efficient Synthesis of Fullerenes in RF Thermal Plasma Reactor. *Chem Phys Lett* **2003**, *378*, 434–439, doi:10.1016/S0009-2614(03)01320-4.

30. Keszler, A.M.; Kováts, É.; Bódis, E.; Károly, Z.; Szépvölgyi, J. Effect of Metallic and Non-Metallic Additives on the Synthesis of Fullerenes in Thermal Plasma. *Condensed Matter 2022, Vol. 7, Page 44* **2022**, *7*, 44, doi:10.3390/CONDMAT7030044.

31. Tong, J.B.; Lu, X.; Liu, C.C.; Pi, Z.Q.; Zhang, R.J.; Qu, X.H. Numerical Simulation and Prediction of Radio Frequency Inductively Coupled Plasma Spheroidization. *Appl Therm Eng* **2016**, *100*, 1198–1206, doi:10.1016/J.APPLTHERMALENG.2016.02.108.

32. Yu, C.; Zhou, X.; Wang, D.; Van Linh, N.; Liu, W. Study on the RF Inductively Coupled Plasma Spheroidization of Refractory W and W-Ta Alloy Powders. *Plasma Science and Technology* **2017**, *20*, 014019, doi:10.1088/2058-6272/AA8E94.

33. Park, J.Y.; Park, K.B.; Kang, J.W.; Kim, H.G.; Hwang, N.M.; Park, H.K. Spheroidization Behavior of Water-Atomized 316 Stainless Steel Powder by Inductively-Coupled Thermal Plasma. *Mater Today Commun* **2020**, *25*, 101488, doi:10.1016/J.MTCOMM.2020.101488.

34. Kim, K.H.; Choi, H.; Han, C. Tungsten Micropowder/Copper Nanoparticle Core/Shell-Structured Composite Powder Synthesized by Inductively Coupled Thermal Plasma Process. *Metall Mater Trans A Phys Metall Mater Sci* **2017**, *48*, 439–445, doi:10.1007/S11661-016-3849-0/METRICS.

35. Dhamale, G.D.; Tak, A.K.; Mathe, V.L.; Ghorui, S. Nucleation and Growth of Y_2O_3 Nanoparticles in a RF-ICTP Reactor: A Discrete Sectional Study Based on CFD Simulation Supported with Experiments. *J Phys D Appl Phys* **2018**, *51*, 255202, doi:10.1088/1361-6463/aac3f1.

36. Oh, J.-W.; Na, H.; Cho, Y.S.; Choi, H. In Situ Synthesis of Bimetallic Tungsten-Copper Nanoparticles via Reactive Radio-Frequency (RF) Thermal Plasma. *Nanoscale Res Lett* **2018**, *13*, 220, doi:10.1186/s11671-018-2623-1.

37. Zhang, X.; Hayashida, R.; Tanaka, M.; Watanabe, T. Synthesis of Carbon-Coated Silicon Nanoparticles by Induction Thermal Plasma for Lithium Ion Battery. *Powder Technol* **2020**, *371*, 26–36, doi:10.1016/J.POWTEC.2020.05.084.

38. Kim, K.S.; Couillard, M.; Shin, H.; Plunkett, M.; Ruth, D.; Kingston, C.T.; Simard, B. Role of Hydrogen in High-Yield Growth of Boron Nitride Nanotubes at Atmospheric Pressure by Induction Thermal Plasma. *ACS Nano* **2018**, *12*, 884–893, doi:10.1021/ACSNANO.7B08708/SUPPL_FILE/NN7B08708_SI_001.PDF.

39. Kim, K.S.; Kingston, C.T.; Ruth, D.; Barnes, M.; Simard, B. Synthesis of High Quality Single-Walled Carbon Nanotubes with Purity Enhancement and Diameter Control by Liquid Precursor Ar–H2 Plasma Spraying. *Chemical Engineering Journal* **2014**, *250*, 331–341, doi:10.1016/J.CEJ.2014.03.117.

40. Li, J.; Hu, R.; Qu, H.; Su, Y.; Wang, N.; Su, H.; Gu, X. Radio-Frequency Thermal Plasma-Induced Novel Chainmail-like Core-Shell MoO2 as Highly Stable Catalyst for Converting Syngas to Higher Alcohols. *Appl Catal B* **2019**, *249*, 63–71, doi:10.1016/J.APCATB.2019.02.060.

41. Takigawa, A.; Kim, T.-H.; Igami, Y.; Umemoto, T.; Tsuchiyama, A.; Koike, C.; Matsuno, J.; Watanabe, T. Formation of Transition Alumina Dust around Asymptotic Giant Branch Stars: Condensation Experiments Using Induction Thermal Plasma Systems. *Astrophys J Lett* **2019**, *878*, L7, doi:10.3847/2041-8213/ab1f80.

42. Tanaka, Y. Recent Development of New Inductively Coupled Thermal Plasmas for Materials Processing. *Adv Phys X* **2021**, *6*, 1867637, doi:10.1080/23746149.2020.1867637.

43. Zhang, H.; Yuan, F.; Chen, Q. Optical Emission Spectroscopy Diagnostics of Atmospheric Pressure Radio Frequency Ar-H2Inductively Coupled Thermal Plasma. *IEEE Transactions on Plasma Science* **2020**, *48*, 3621–3628, doi:10.1109/TPS.2020.3023689.

44. Tu, X.; Chéron, B.G.; Yan, J.H.; Cen, K.F. Electrical and Spectroscopic Diagnostic of an Atmospheric Double Arc Argon Plasma Jet. *Plasma Sources Sci Technol* **2007**, *16*, 803, doi:10.1088/0963-0252/16/4/016.

45. Nikiforov, A.Y.; Leys, C.; Gonzalez, M.A.; Walsh, J.L. Electron Density Measurement in Atmospheric Pressure Plasma Jets: Stark Broadening of Hydrogenated and Non-Hydrogenated Lines. *Plasma Sources Sci Technol* **2015**, *24*, 034001, doi:10.1088/0963-0252/24/3/034001.

46. Chen, C.; Fu, W.; Zhang, C.; Lu, D.; Han, M.; Yan, Y. Langmuir Probe Diagnostics with Optical Emission Spectrometry (OES) for Coaxial Line Microwave Plasma. *Applied Sciences 2020, Vol. 10, Page 8117* **2020**, *10*, 8117, doi:10.3390/APP10228117.

47. Wu, J.; Zhang, P.; Yu, D.; Zhang, S.; Xin, Q.; Wan, Y. Monitoring and Diagnosis of the Inductively Coupled Atmospheric Pressure Plasma Jet for Deterministic Optical Processing. *Optik (Stuttg)* **2020**, *214*, 164815, doi:10.1016/j.ijleo.2020.164815.

48. Galiwango, E.; A.Gabbar, H. Synergistic Interactions, Kinetic and Thermodynamic Analysis of Co-Pyrolysis of Municipal Paper and Polypropylene Waste. *Waste Management* **2022**, *146*, 86–93, doi:10.1016/j.wasman.2022.04.032.

49. Ganguli, A.; Tarey, R. Understanding Plasma Sources. *Curr Sci* **2002**, *83*, 279–290.

50. Aldeeb, M.A.; Morgan, N.; Abouelsayed, A.; Amin, K.M.; Hassaballa, S. Electrical and Optical Characterization of Acetylene RF CCP for Synthesis of Different Forms of Hydrogenated Amorphous Carbon Films. *Plasma Chemistry and Plasma Processing* **2020**, *40*, 387–406, doi:10.1007/S11090-019-10031-8/METRICS.

51. OHNO, N.; RAZZAK, M.A.; UKAI, H.; TAKAMURA, S.; UESUGI, Y. Validity of Electron Temperature Measurement by Using Boltzmann Plot Method in Radio Frequency Inductive Discharge in the Atmospheric Pressure Range. *Plasma and Fusion Research* **2006**, *1*, 028–028, doi:10.1585/pfr.1.028.

52. Abbass, Q.; Ahmed, N.; Ahmed, R.; Baig, M.A. A Comparative Study of Calibration Free Methods for the Elemental Analysis by Laser Induced Breakdown Spectroscopy. *Plasma Chemistry and Plasma Processing* **2016**, *36*, 1287–1299, doi:10.1007/s11090-016-9729-y.

53. Tu, X.; Chéron, B.G.; Yan, J.H.; Cen, K.F. Electrical and Spectroscopic Diagnostic of an Atmospheric Double Arc Argon Plasma Jet. *Plasma Sources Sci Technol* **2007**, *16*, 803–812, doi:10.1088/0963-0252/16/4/016.

54. Younus, M.; Rehman, N.U.; Shafiq, M.; Naeem, M.; Zaka-Ul-Islam, M.; Zakaullah, M. Evolution of Plasma Parameters in an Ar–N $_2$ /He Inductive Plasma Source with Magnetic Pole Enhancement. *Plasma Science and Technology* **2017**, *19*, 025402, doi:10.1088/2058-6272/19/2/025402.

55. OHNO, N.; RAZZAK, M.A.; UKAI, H.; TAKAMURA, S.; UESUGI, Y. Validity of Electron Temperature Measurement by Using Boltzmann Plot Method in Radio Frequency Inductive Discharge in the Atmospheric Pressure Range. *Plasma and Fusion Research* **2006**, *1*, 028–028, doi:10.1585/pfr.1.028.

56. Godyak, V.A. Electrical and Plasma Parameters of ICP with High Coupling Efficiency. *Plasma Sources Sci Technol* **2011**, *20*, 025004, doi:10.1088/0963-0252/20/2/025004.

57. Godyak, V.A.; Piejak, R.B.; Alexandrovich, B.M. Electron Energy Distribution Function Measurements and Plasma Parameters in Inductively Coupled Argon Plasma. *Plasma Sources Sci Technol* **2002**, *11*, 525–543, doi:10.1088/0963-0252/11/4/320.

58. Jun-Feng, Z.; Xin-Chao, B.; Qiang, C.; Fu-Ping, L.; Zhong-Wei, L. Diagnosis of Methane Plasma Generated in an Atmospheric Pressure DBD Micro-Jet by Optical Emission Spectroscopy. *Chinese Physics Letters* **2009**, *26*, 035203, doi:10.1088/0256-307X/26/3/035203.

59. Kolobov, V. The Anomalous Skin Effect in Bounded Systems. In *Electron Kinetics and Applications of Glow Discharges*; Kluwer Academic Publishers: Boston; pp. 293–311.

60. Nikiforov, A.Y.; Leys, C.; Gonzalez, M.A.; Walsh, J.L. Electron Density Measurement in Atmospheric Pressure Plasma Jets: Stark Broadening of Hydrogenated and Non-Hydrogenated Lines. *Plasma Sources Sci Technol* **2015**, *24*, 034001, doi:10.1088/0963-0252/24/3/034001.

61. Sadeghzadeh Lari, E.; Ranjbar Askari, H.; Meftah, M.T.; Shariat, M. Calculation of Electron Density and Temperature of Plasmas by Using New Stark Broadening Formula of Helium Lines. *Phys Plasmas* **2019**, *26*, 023519, doi:10.1063/1.5085050.

62. Sadeghzadeh Lari, E.; Ranjbar Askari, H.; Meftah, M.T.; Shariat, M. Calculation of Electron Density and Temperature of Plasmas by Using New Stark Broadening Formula of Helium Lines. *Phys Plasmas* **2019**, *26*, doi:10.1063/1.5085050.

63. Nijdam, S.; Teunissen, J.; Ebert, U. The Physics of Streamer Discharge Phenomena. *Plasma Sources Sci Technol* **2020**, *29*, 103001, doi:10.1088/1361-6595/abaa05.

64. Tamošiūnas, A.; Valatkevičius, P.; Valinčius, V.; Grigaitienė, V.; Kavaliauskas, Ž. Diagnostic Methods Used for Atmospheric Pressure Thermal Arc Plasma. *Phys Scr* **2014**, *T161*, 014059, doi:10.1088/0031-8949/2014/T161/014059.

65. Ali, A.M.; Abu Hassan, M.A.; Ibrahim, R.R.K.; Jalil, A.A.; Mat Nayan, N.H.; Abdulkarim, B.I.; Sabeen, A.H. Analysis of Solid Residue and Flue Gas from Thermal Plasma Treatment of Petroleum Sludge. *J Environ Chem Eng* **2019**, *7*, 103207, doi:10.1016/J.JECE.2019.103207.

66. Bhatt, K.P.; Patel, S.; Upadhyay, D.S.; Patel, R.N. A Critical Review on Solid Waste Treatment Using Plasma Pyrolysis Technology. *Chemical Engineering and Processing - Process Intensification* **2022**, *177*, 108989, doi:10.1016/J.CEP.2022.108989.

67. Cai, X.; Cai, H.; Shang, C.; Du, C. Two-Stage Pyrolysis/Gasification and Plasma Conversion Technology for the Utilization of Solid Waste. *IEEE Transactions on Plasma Science* **2021**, *49*, 191–213, doi:10.1109/TPS.2020.3044534.